Fluid-particle flow modelling and validation using two-way-coupled mesoscale SPH-DEM

Martin Robinson[a,*], Stefan Luding[a], Marco Ramaioli[b]

[a] *Multiscale Mechanics, University of Twente, Enschede, Netherlands*
[b] *Nestlé Research Center, Lausanne, Switzerland*

Abstract

We present a meshless simulation method for multiphase fluid-particle flows coupling Smoothed Particle Hydrodynamics (SPH) and the Discrete Element Method (DEM). Rather than fully resolving the interstitial fluid, which is often infeasible, the unresolved fluid model is based on the locally averaged Navier Stokes equations, which are coupled with a DEM model for the solid phase. In contrast to similar mesh-based Discrete Particle Methods (DPMs), this is a purely particle-based method and enjoys the flexibility that comes from the lack of a prescribed mesh. It is suitable for problems such as free surface flow or flow around complex, moving and/or intermeshed geometries. It can be used for both one and two-way coupling and is applicable to both dilute and dense particle flows. A comprehensive validation procedure for fluid-particle simulations is presented and applied to the SPH-DEM method, using simulations of single and multiple particle sedimentation in a 3D fluid column and comparison with analytical models. Millimetre-sized particles are used along with three different test fluids: air, water and a water-glycerol solution. The velocity evolution for the single particle compares well (less than 2% error) with the analytical solution as long as the fluid resolution is coarser than 2 times the particle diameter. The multiple particle sedimentation problems (sedimentation of a homogeneous porous block and a Rayleigh Taylor instability) also reproduce the expected

*Corresponding author
Email addresses: m.j.robinson@utwente.nl (Martin Robinson), s.luding@utwente.nl (Stefan Luding), Marco.Ramaioli@rdls.nestle.com (Marco Ramaioli)

terminal velocity well for porosities $0.5 \leq \epsilon \leq 1.0$, but although care should be taken in the presence of high porosity gradients. Overall the SPH-DEM method successfully reproduces the expected behaviour in the sedimentation test cases, and promises to be a flexible and accurate tool for other fluid-particle system simulations.
Keywords: SPH, DEM, Fluid-particle flow, Discrete Particle Model, Sedimentation, Rayleigh-Taylor instability

1. Introduction

Fluid-particle systems are ubiquitous in nature and industry. Sediment transport and erosion are important in many environmental studies and the interaction between particles and interstitial fluid affects the rheology of avalanches, slurry flows and soils. In industry, the efficiency of a fluidised bed process (e.g. Fluidized Catalytic Cracking) is completely determined by the complex two-way interaction between the injected gas flow and the solid granular material. Also, the dispersion of solid particles in a fluid is of broad industrial relevance to the food, chemical and painting industries, which involves in most cases three phases: a granular medium, the air initially present in its pores and an injected liquid.

The length-scale of interest determines the method of simulation for fluid-particle systems. For very small scale processes it is feasible to fully resolve the interstitial fluid between the particles (see Zhu et al. (1999); Pereira et al. (2010); Potapov (2001); Wachmann et al. (1998) for a few examples of particle or pore-scale simulations). However, for many applications the dynamics of interest occur over length scales much larger than the particle diameter and the computational effort required to resolve the pore-scale is too great. It then becomes necessary to use unresolved, or mesoscale, fluid simulations. This mesoscale is the focus of this paper and the domain of applicability for the SPH-DEM method. At even larger length scales of interest (macroscale) it becomes infeasible to model the granular material as a discrete collection of grains

and instead a continuum model is used in a two-fluid model. However, it must be noted that while this approach might be computationally necessary in many cases, it can fail for some systems involving dense granular flow, where existing continuum models for granular material do not adequately reproduce important material properties such as anisotropy, history dependency, jamming and segregation.

Fluid-particle simulations at the mesoscale are often given the term Discrete Particle Models (DPM). These models fully resolve the individual solid particles using a Lagrangian model for the solid phase. The fluid phase does not resolve the interstitial fluid, but instead models the locally averaged Navier-Stokes equations and is coupled to the solid particles using appropriate drag closures. Most of the prior work on DPMs have been done using grid-based methods for the fluid phase, and a few relevant examples can be seen in the papers by Tsuji et al. (1993), Xu (1997, 2000), Hoomans (1996); Hoomans et al. (2000) or Chu and Yu (2008).

Fixed pore flow simulations (where the geometry of the solid particles is unchanging over time) using SPH for the (unresolved) fluid phase have been described by Li et al. (2007) and Jiang et al. (2007), but these do not allow for the motion and collision of solid grains. Cleary et al. (2006) and Fernandez et al. (2011) simulate slurry flow at the mesoscale using SPH and DEM in SAG mills and through industrial banana screens, but only perform a one-way coupling between the solid and fluid phases.

The DPM model presented in this paper is based on the locally averaged Navier-Stokes (AVNS) equations that were first derived by Anderson and Jackson in the sixties (Anderson and Jackson, 1967), and have been used with great success to model the complex fluid-particle interactions occurring in industrial fluidized beds (Deen et al., 2007). Anderson and Jackson defined a smoothing operator identical to that used in SPH and used it to reformulate the NS equations in terms of smoothed variables and a local porosity field (porosity refers to the fraction of fluid in a given volume). Given its theoretical basis in kernel interpolation, it is natural to consider the use of the SPH method to solve the

AVNS equations, coupled with a DEM model for the solid phase.

The coupling of SPH and DEM results in a purely particle-based solution method and therefore enjoys the flexibility that is inherent in these methods. This is the primary advantage of this method over existing grid-based DPMs. In particular, the model described in this paper is well suited for applications involving a free surface, including (but not limited to) debris flows, avalanches, landslides, sediment transport or erosion in rivers and beaches, slurry transport in industrial processes (e.g. SAG mills) and liquid-powder dispersion and mixing in the food processing industry.

Another advantage of using a DPM, or mesoscale simulation, is of course the reduced computational requirements over a fully resolved simulation. For example, we have found that in general a fluid resolution of $h = 2d$ minimises the error in the SPH-DEM method, where d is the solid particle diameter. For a fully resolved simulation the interstitial fluid must be resolved, and therefore the fluid resolution would need to be at least $h = 0.2d$, which scales the number of computational nodes (for the fluid) by a factor of 1000.

Figure 1 shows a SPH-DEM simulation applied to a liquid-powder mixing problem in the food processing industry, taken from a simulation of a water jet injected in a granular bed whose pores are initially filled with air. To predict the shape of the front correctly, one has to consider the free surface and the absence of dissipation on the air side, both included in the SPH-DEM model. Even more complex (realistic) injection geometries are easily incorporated into the simulation with no additional effort. Moreover, using DEM enables studying the effect (on the initial liquid front propagation) of packing and top surface inhomogeneities that can be generated during pouring, unlike simpler "porous media"-like approaches. Polydispersity can also be included by altering the radius of the simulated grains and using an applicable drag term (e.g. see Van der Hoef et al. (2005))

Sections 2-3 describes the AVNS equations and the SPH and DEM models for the fluid and solid phases and the coupling between them. Section 4 introduces the test cases, Section 5 describes the results for the Single Particle

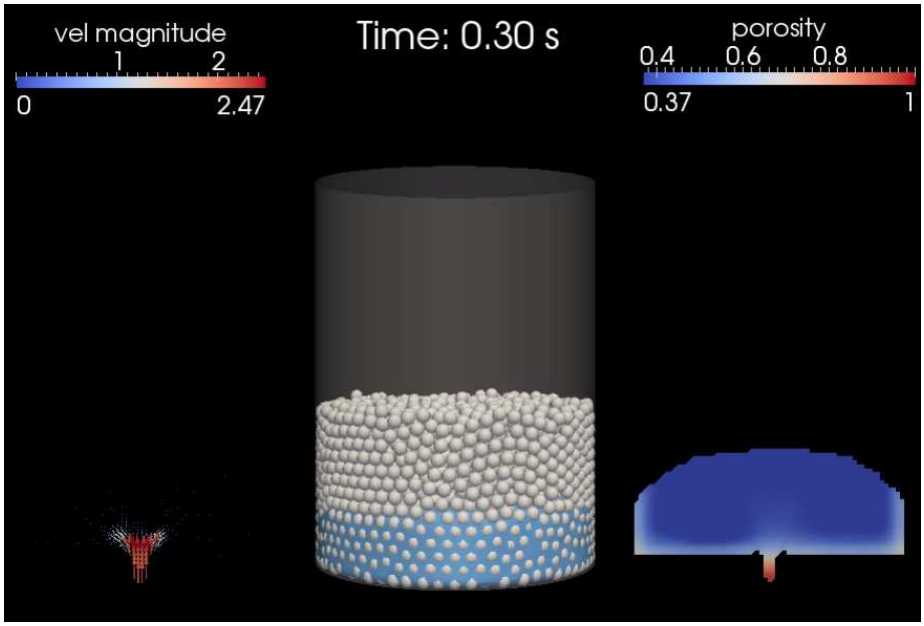

Figure 1: Example of a two-phase SPH-DEM simulation of a water jet (bottom) injected into a granular bed.

Sedimentation test case, Section 6 the results for Multiple Particle Sedimentation and Section 7 describes the simulation of a Rayleigh Taylor Instability using solid particles sedimenting into a clear fluid.

2. Governing Equations

2.1. The Locally Averaged Navier-Stokes Equations

Here we describe the governing equations for the fluid phase, the locally averaged Navier-Stokes equations derived by Anderson and Jackson (1967). Anderson and Jackson defined a local averaging based on a radial smoothing function $g(r)$. The function $g(r)$ is greater than zero for all r and decreases monotonically with increasing r, it possesses derivatives $g^n(r)$ of all orders and is normalised so that $\int g(r)dV = 1$.

The local average of any field a' defined over the fluid domain can be obtained by convolution with the smoothing function

$$\epsilon(x)a(x) = \int_{V_f} a'(y)g(x-y)dV_y, \tag{1}$$

where x and y are position coordinates (here one dimensional for simplicity). The integral is taken over the volume of interstitial fluid V_f and $\epsilon(x)$ is the porosity.

$$\epsilon(x) = 1 - \int_{V_s} g(x-y)dV_y, \tag{2}$$

where V_s is the volume of the solid particles.

In a similar fashion, the local average of any field $a'(x)$ defined over the solid domain is given by

$$(1-\epsilon(x))a(x) = \int_{V_s} a'(y)g(x-y)dV_y, \tag{3}$$

where the integral is taken over the volume of the solid particles.

Applying this averaging method to the Navier-Stokes equations, Anderson and Jackson (1967) derived the following continuity equation in terms of locally averaged variables

$$\frac{\partial(\epsilon\rho_f)}{\partial t} + \nabla\cdot(\epsilon\rho_f\mathbf{u}) = 0, \tag{4}$$

where ρ_f is the fluid mass density and $\mathbf{u}$ is the fluid velocity.

The corresponding momentum equation is

$$\epsilon\rho_f\left(\frac{\partial\mathbf{u}}{\partial t} + \mathbf{u}\cdot\nabla\mathbf{u}\right) = -\nabla P + \nabla\cdot\boldsymbol{\tau} - n\mathbf{f} + \epsilon\rho_f\mathbf{g}, \tag{5}$$

where P is the fluid pressure, $\boldsymbol{\tau}$ is the viscous stress tensor and $n\mathbf{f}$ is the fluid-particle coupling term. We use a Newtonian fluid where $\boldsymbol{\tau} = \mu\nabla\cdot\mathbf{u}$. We neglect Reynolds-like terms and do not consider turbulent flow. The coefficient for the coupling term n is the local average of the number of particles per unit volume and $\mathbf{f}$ is the local mean value of the force exerted on the particles by the fluid. This force includes all effects, both static and dynamic, of the particles on the fluid, the details of which can be seen in Eq. (23).

2.2. Smoothed Particle Hydrodynamics

Smoothed Particle Hydrodynamics (Gingold and Monaghan, 1977; Lucy, 1977; Monaghan, 2005) is a Lagrangian scheme, whereby the fluid is discretised into "particles" that move with the local fluid velocity. Each particle is assigned a mass and can be thought of as the same volume of fluid over time. The fluid variables and the equations of fluid dynamics are interpolated over each particle and its nearest neighbours using a smoothing kernel $W(r, h)$, where h is the smoothing length scale. Like $g(r)$ in the AVNS equations, the SPH kernel is a radial function that decreases monotonically and is normalised so that $\int W(r, h)dV = 1$.

Unlike $g(r)$ and to reduce the computational burden of the method, the SPH kernel is normally defined with a compact support and a finite number of derivatives.

In SPH, a fluid variable $A(\mathbf{r})$ (such as momentum or density) is interpolated using the kernel W

$$A(\mathbf{r}) = \int A(\mathbf{r}')W(\mathbf{r} - \mathbf{r}', h)d\mathbf{r}'. \tag{6}$$

To apply this to the discrete SPH particles, the integral is replaced by a sum over all particles, commonly known as the *summation interpolant*. To estimate the value of the function A at the location of particle a (denoted as A_a), the summation interpolant becomes

$$A_a = \sum_b m_b \frac{A_b}{\rho_b} W_{ab}(h_a), \tag{7}$$

where m_b and ρ_b are the mass and density of particle b. The volume element $d\mathbf{r}'$ of Eq. (6) has been replaced by the volume of particle b (approximated by $\frac{m_b}{\rho_b}$), equivalent to the normal trapezoidal quadrature rule. The kernel function is denoted by $W_{ab}(h) = W(\mathbf{r}_a - \mathbf{r}_b, h)$. The dependence of the kernel on the difference in particle positions is not explicitly stated for readability. Due to the limited support of W, particle neighbourhood search methods as standard in SPH or DEM can be applied to optimize the summation in Eq. (6).

The accuracy of the SPH interpolant depends on the particle positions within the radius of the kernel. If there is not a homogeneous distribution of particles around particle a (for example, it is on a free surface), then the interpolation can be compromised.

The interpolation can be improved by using a Shepard correction (Shepard, 1968), originally devised as a low cost improvement to data fitting. This correction divides the interpolant by the sum of kernel values at the SPH particle positions, so the summation interpolant becomes

$$A_a = \frac{1}{\sum_b \frac{m_b}{\rho_b} W_{ab}(h_a)} \sum_b m_b \frac{A_b}{\rho_b} W_{ab}(h_a). \tag{8}$$

This correction ensures that a constant field will always be interpolated exactly, and improves the interpolation accuracy of other, non-constant fields.

3. SPH-DEM Model

3.1. SPH implementation of the AVNS equations

SPH is based on a similar local averaging technique as the AVNS equations, so it is natural to convert the interpolation integrals in Eqs. (1) and (2) to SPH sums using a smoothing kernel $W(r, h)$ in place of $g(r)$.

To calculate the porosity ϵ_a at the center position of SPH/DEM particle a, the integral in Eq. (2) is converted into a sum over all DEM particles within the kernel radius and becomes

$$\epsilon_a = 1 - \sum_j W_{aj}(h_c) V_j, \tag{9}$$

where V_j is the volume of DEM particle j. For readability, sums over SPH particles use the subscript b, while sums over surrounding DEM particles use the subscript j. Note that we have used a coupling smoothing length h_c to evaluate the porosity, which sets the length scale for the coupling terms between the phases. Here we set h_c to be equal to the SPH smoothing length, but in practice this can be set within a range such that h_c is large enough that the porosity field is smooth but small enough to resolve the important features of

the porosity field. For more details on this point please consult the numerical results of the test cases and the conclusions of this paper.

Applying the local averaging method to the Navier-Stokes equations, Anderson and Jackson derived the continuity and momentum equations shown in Eqs. (4) and (5) respectively. To convert these to SPH equations, we first define a superficial fluid density ρ equal to the intrinsic fluid density scaled by the local porosity $\rho = \epsilon\rho_f$.

Substituting the superficial fluid density into the averaged continuity and momentum equations reduces them to the normal Navier-Stokes equations. Therefore, our approach is to use the standard weakly compressible SPH equations, see (Robinson and Monaghan, 2011), using the superficial density for the SPH particle density and adding terms to model the fluid-particle drag.

The rate of change of superficial density is calculated using the variable smoothing length terms derived by Price (2012)

$$\frac{D\rho_a}{Dt} = \frac{1}{\Omega_a}\sum_b m_b \mathbf{u}_{ab}\cdot\nabla_a W_{ab}(h_a), \tag{10}$$

where the capitals in the time derivative denote the material derivative. $\mathbf{u}_{ab} = \mathbf{u}_a - \mathbf{u}_b$ and Ω_a is a correction factor due to the gradient of the smoothing length

$$\Omega_a = 1 - \frac{\partial h_a}{\partial \rho_a}\sum_b m_b \frac{\partial W_{ab}(h_a)}{\partial h_a}. \tag{11}$$

Neglecting gravity, the SPH acceleration equation becomes

$$\frac{d\mathbf{u}_a}{dt} = -\sum_b m_b\left[\left(\frac{P_a}{\Omega_a\rho_a^2}+\Pi_{ab}\right)\nabla_a W_{ab}(h_a) + \left(\frac{P_b}{\Omega_b\rho_b^2}+\Pi_{ab}\right)\nabla_a W_{ab}(h_b)\right] + \mathbf{f}_a/m_a, \tag{12}$$

where $\mathbf{f}_a$ is the coupling force on the SPH particle a due to the DEM particles (see Section 3.3). The viscous term Π_{ab} models the divergence of the viscous stress tensor in Eq. (5) is calculated using the term proposed by Monaghan

(1997), which is based on the dissipative term in shock solutions based on Riemann solvers. For this viscosity

$$\Pi_{ab} = -\alpha \frac{u_{sig} u_n}{2\overline{\rho}_{ab} |\mathbf{r}_{ab}|}, \tag{13}$$

where $u_{sig} = c_s + u_n/|\mathbf{r}_{ab}|$ is a signal velocity that represents the speed at which information propagates between the particles. The normal velocity difference between the two particles is given by $u_n = \mathbf{u}_{ab} \cdot \mathbf{r}_{ab}$. The constant α can be related to the dynamic viscosity of the fluid μ using

$$\mu = \rho \alpha h c_s / S, \tag{14}$$

where $S = 112/15$ for two dimensions and $S = 10$ for three (Monaghan, 2005). For some of the reference fluids we have chosen to simulate in this paper it was found that the physical viscosity was not sufficient to stabilise the results (see Section 6.3), and it was necessary to add an artificial viscosity term with $\alpha_{art} = 0.1$. However, this viscosity term is only applied when the SPH particles are approaching each other (i.e. $u_{ab} \cdot r_{ab} < 0$) so that the dissipation due to the artificial viscosity is reduced while still stabilising the results.

The fluid pressure in Eq. (12) is calculated using the weakly compressible equation of state. This equation of state defines a reference density ρ_0 at which the pressure vanishes, which must be scaled by the local porosity to ensure that the pressure is constant over varying porosity.

$$P_a = B \left(\left(\frac{\rho_a}{\epsilon_a \rho_0} \right)^{\gamma} - 1 \right). \tag{15}$$

The scaling factor B, is free a-priori and is set so that the density variation from the local reference density is less than 1 percent, ensuring that the fluid is close to incompressible. For this, in terms of B, the local sound speed is

$$c_s^2 = \left. \frac{\partial P}{\partial \overline{\rho}} \right|_{\overline{\rho} = \epsilon_a \rho_0} = \frac{\gamma B}{\epsilon_a \rho_0}, \tag{16}$$

and the fluctuations in density can be related to the sound speed and velocity of the particles (Monaghan, 2005):

$$\frac{|\delta\rho|}{\rho} = \frac{u^2}{c_s^2}. \tag{17}$$

Therefore, in order to keep these fluctuations less than 1% in a flow where the maximum velocity is u_m and the maximum porosity is as always $\epsilon_m = 1$, B is set to

$$B = \frac{100\rho_0 u_m^2}{\gamma}. \tag{18}$$

As the superficial density will vary according to the local porosity, care must be taken to update the smoothing length for all particles in order to maintain a sufficient number of neighbour particles. This is referred to as "variable-h" in this study. The smoothing length h_a is calculated using

$$h_a = \sigma \left(\frac{m_a}{\rho_a} \right)^{1/d}, \tag{19}$$

where d is the number of dimensions and σ determines the resolution of the summation interpolant. The value used in all the simulation results presented here is $\sigma = 1.5$.

Recall that the SPH density is given by $\rho = \epsilon\rho_f$. Assuming a constant intrinsic fluid density ρ_f, the smoothing length h is thus proportional to the local porosity $h \propto (1/\epsilon)^{1/d}$.

3.2. Discrete Element Model (DEM)

In DEM (also known as Molecular Dynamics), Newton's equations of motion are integrated for each individual solid particle. Interactions between the particles involve explicit force expressions that are used whenever two particles come into contact.

Given a DEM particle i with position $\mathbf{r}_i$, the equation of motion is

$$m_i \frac{d^2\mathbf{r}_i}{dt^2} = \sum_j \mathbf{c}_{ij} + \mathbf{f}_i + m_i\mathbf{g}, \tag{20}$$

where m_i is the mass of particle i, $\mathbf{c}_{ij}$ is the contact force between particles i and j (acting from j to i) and $\mathbf{f}_i$ is the fluid-particle coupling force on particle

i. For the simulations presented below, we have used the linear spring dashpot contact model

$$\mathbf{c}_{ij} = -(k\delta - \beta\dot{\delta})\mathbf{n}_{ij}, \tag{21}$$

where δ is the overlap between the two particles (positive when the particles are overlapping, zero when they are not) and $\mathbf{n}_{ij}$ is the unit normal vector pointing from j to i.. The simulation timestep is calculated based on a typical contact duration t_c and is given by $\Delta t = \frac{1}{50}t_c$, with $t_c = \pi/\sqrt{(2k/m_i) - \beta/m_i}$.

The timestep for the SPH method is set by a CFL condition

$$\delta t_1 \leq \min_a \left(0.6\frac{h_a}{u_{sig}}\right), \tag{22}$$

where the minimum is taken over all the particles. This is normally much larger than the DEM contact time, so the DEM timestep usually sets the minimum timestep for the SPH-DEM method.

See Table 1 for all the parameters and time-scales used in these simulations.

3.3. Fluid-Particle Coupling Forces

The force on each solid particle by the fluid is (Anderson and Jackson, 1967)

$$\mathbf{f}_i = V_i(-\nabla P + \nabla \cdot \tau)_i + \mathbf{f}_d(\epsilon_i, \mathbf{u}_s), \tag{23}$$

where V_i is the volume of particle i. The first two terms models the effect of the resolved fluid forces (buoyancy and shear-stress) on the particle. For a fluid in hydrostatic equilibrium, the pressure gradient will reduce to the buoyancy force on the particle. The divergence of the shear stress is included for completeness and ensures that the movement of a neutrally buoyant particle will follow the fluid streamlines. For the simulations considered in this paper this term will not be significant.

The force $\mathbf{f}_d$ is a particle drag force that depends on the local porosity ϵ_i and the superficial velocity $\mathbf{u}_s$ (defined in the following section). This force models the drag effects of the unresolved fluctuations in the fluid variables and

is normally defined using both theoretical arguments and fits to experimental data. For a single particle in 3D creeping flow this term would be the standard Stokes drag force. For higher Reynolds numbers and multiple particle interactions this term is determined using fits to numerical or experimental data (Van der Hoef et al., 2005). See Section 3.4 for further details.

The pressure gradient and the divergence of the stress tensor are evaluated at each solid particle using a Shepard corrected (Shepard, 1968) SPH interpolation. Using the already given SPH acceleration equation, Eq. (12), this becomes

$$(-\nabla P + \nabla \cdot \tau)_i = \frac{1}{\sum_b \frac{m_b}{\rho_b} W_{ab}(h_b)} \sum_b m_b \theta_b W_{ib}(h_b), \tag{24}$$

$$\theta_a = -\sum_b m_b \left[\left(\frac{P_a}{\Omega_a \rho_a^2} + \Pi_{ab} \right) \nabla_a W_{ab}(h_a) + \left(\frac{P_b}{\Omega_b \rho_b^2} + \Pi_{ab} \right) \nabla_a W_{ab}(h_b) \right]. \tag{25}$$

In order to satisfy Newtons third law (i.e. the action = reaction principle), the fluid-particle coupling force on the fluid must be equal and opposite to the force on the solid particles. Each DEM particle is contained within multiple SPH interaction radii, so care must be taken to ensure that the two coupling forces are balanced.

The coupling force on SPH particle a is determined by a weighted average of the fluid-particle coupling force on the surrounding DEM particles. The contribution of each DEM particle to this average is scaled by the value of the SPH kernel.

$$\mathbf{f}_a = -\frac{m_a}{\rho_a} \sum_j \frac{1}{S_j} \mathbf{f}_j W_{aj}(h_c), \tag{26}$$

where $\mathbf{f}_j$ is the coupling force calculated for each DEM particle using Eq. (23). The scaling factor S_j is added to ensure that the force on the fluid phase exactly balances the force on the solid particles. It is given by

$$S_j = \sum_b \frac{m_b}{\rho_b} W_{jb}(h_c), \tag{27}$$

where the sum is taken over all the SPH particles surrounding DEM particle j. For a DEM particle immersed in the fluid this will be close to unity.

3.4. Fluid-Particle Drag Laws

The drag force $\mathbf{f}_d$ depends on the superficial velocity $\mathbf{u}_s$, which is proportional to the relative velocity between the phases. If $\mathbf{u}_f$ and $\mathbf{u}_i$ are the fluid and particle velocity respectively, then the superficial velocity is defined as $\mathbf{u}_s = \epsilon_i(\mathbf{u}_f - \mathbf{u}_i)$. This term is used as the dependent variable in many drag laws as it is easily measured from experiment by dividing the fluid flow rate by the cross-sectional area.

In the SPH-DEM model, the fluid velocity $\mathbf{u}_f$ used to calculate the superficial velocity, is found at each DEM particle position using a Shepard corrected SPH interpolation. The value of the porosity field at each DEM particle position ϵ_i is found in an identical way.

The simplest drag law is the Stokes drag force

$$\mathbf{f}_d = 3\pi\mu d\mathbf{u}_s, \tag{28}$$

where d is the particle diameter. This is valid for a single particle in creeping flow.

Coulson and Richardson (1993) proposed a drag law valid for a single particle falling under the full range of particle Reynolds Numbers $Re_p = \rho_f|\mathbf{u}_s|d/\mu$.

$$\mathbf{f}_d = \frac{\pi}{4}d^2\rho_f|\mathbf{u}_s|\left(1.84Re_p^{-0.31} + 0.293Re_p^{0.06}\right)^{3.45} \tag{29}$$

For higher Reynolds numbers and multiple particles, the drag law can be generalised to

$$\mathbf{f}_d = \frac{1}{8}C_d f(\epsilon_i)\pi d^2\rho_f|\mathbf{u}_s|\mathbf{u}_s, \tag{30}$$

where C_d is a drag coefficient that varies with the particle Reynolds number $Re_p = \rho_f|\mathbf{u}_s|d/\mu$, and $f(\epsilon_i)$ is the voidage function that models the interactions between multiple particles in the fluid.

A popular definition for the drag coefficient was proposed by Dallavalle (1948)

$$C_d = \left[0.63 + \frac{4.8}{\sqrt{Re_p}}\right]^2. \tag{31}$$

Di Felice proposed a voidage function based on experimental data of fluid flow through packed spheres (Di Felice, 1994)

$$f(\epsilon_i) = \epsilon_i^{-\xi}, \tag{32}$$

$$\xi = 3.7 - 0.65 \exp\left[-\frac{(1.5 - \log_{10} Re_p)^2}{2}\right]. \tag{33}$$

Both the Stokes drag term (as the simplest reference case) and the combination of Dallavalle and Di Felice's drag terms are used in the simulations presented in this paper. Another commonly used drag term is given by a combination of drag terms by Ergun (1952) and Wen and Yu (1966). For $\epsilon_i \to 1$ this term and Di Felice's are identical (over all Re). As the porosity decreases both drag terms generally follow the same trend, although the Ergun and Wen & Yu model gives a larger drag force for dense systems.

4. Validation Test Cases

Three different sedimentation test cases were used to verify that SPH-DEM correctly models the dynamics of the two phases (fluid and solid particles) and their interactions.

1. Single Particle Sedimentation (SPS)
2. Sedimentation of a constant porosity block (CPB)
3. Rayleigh Taylor Instability (RTI)

These test cases were designed to test the particle-fluid coupling mechanics in order of increasing complexity. The first test case simply requires the correct calculation and integration of the drag force on the single particle, the single particle being too small to noticeably alter the surrounding fluid velocity. The

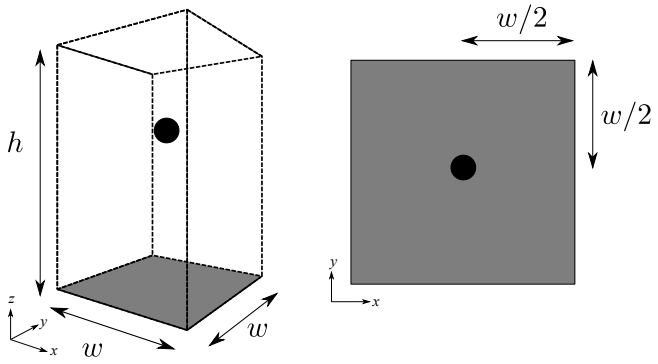

Figure 2: Setup for test case SPS, single particle sedimentation in a fluid column. (Left) Perspective view, showing the fluid domain, the no-slip bottom boundary and the single spherical DEM particle. (Right) Top view, the grey area is the bottom no-slip boundary

second requires that the drag on both phases and the displacement of fluid by the particles be correctly modelled for a simple velocity field and constant porosity. The third test case does the same but with a more complicated and time-varying velocity and porosity field.

The first test case (SPS) models a single particle sedimenting in a fluid column under gravity. Figure 2 shows a diagram of the simulation domain. The water column has a height of $h = 0.006$m and the bottom boundary is constructed using Lennard-Jones repulsive particles (these particles are identical to those used by Monaghan et al. (2003)). The boundaries in the x and y directions are periodic with a width of $w = 0.004$ m and gravity acts in the negative z direction. The single DEM particle is initialised at $z = 0.8h$. It has a diameter equal to $d = 1 \times 10^{-4}$ m and has a density $\rho_p = 2500$ kg/m^3.

For the initial conditions of the simulation, the position of the DEM particle is fixed and the fluid is allowed to reach hydrostatic equilibrium. The particle is then released at $t = 0$ s.

Most fluid-particle systems of interest will involve large numbers of particles, and therefore the second test case (CPB) involves the sedimentation of multiple particles through a water column. In this case, a layer of sedimenting particles is placed above a clear fluid region. Figure 3 shows the setup geometry. The fluid column is identical to the previous test case, but now the upper half of the

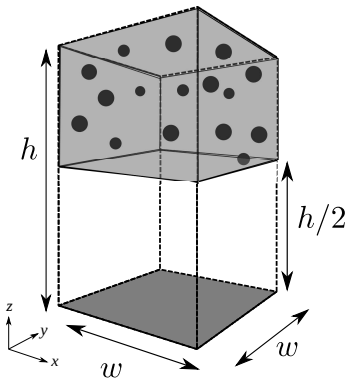

Figure 3: Setup for test cases CPB and RTI, multiple particle sedimentation in a fluid column.

column is occupied by regularly distributed DEM particles on a square cubic lattice, with a given porosity ϵ. The separation between adjacent DEM particles on the lattice is given by $\Delta r = (V/(1-\epsilon))^{1/3}$, where V is the (constant) particle volume. The diameter and density of the particles are identical to the single particle case. In order to maintain a constant porosity as the layer of particles falls, the DEM particles are restricted from moving relative to each other and the layer of particles falls as a block (only translation, no rotation of the layer).

The third test cases (RTI) uses the same simulation domain and initial conditions as CPB, but now the particles are allowed to move freely. This setup is similar in nature to the classical Rayleigh-Taylor (RT) instability, where a dense fluid is accelerated (normally via gravity) into a less dense fluid. The combination of particles and fluid can be modeled as a two-fluid system with the upper "fluid" having an effective density ρ_d, and an effective viscosity μ_d, both higher than the properties of the fluid without particles. From this an expected growth rate can be calculated for the instability and compared with the simulated growth rate. See Section 7 for more details.

For all three test cases, three different model fluids are used to evaluate the SPH-DEM model at different fluid viscosities and particle Reynolds numbers. The density and viscosities of these fluids correspond to the physical properties of air, water and a 10% glycerol-water solution.

4.1. Simulation Parameters and Timescales

Table 1 shows the parameters used in the three test cases. Each column corresponds to a different model fluid. Where a value appears only in one column, this indicates that the parameter is constant for all the fluids. The particle Reynolds number is calculated using the expected terminal velocity of the single particle or multiple particle block.

The standard Stokes law, Eq. (28), can be used to calculate the vertical speed of a single particle falling in a quiescent fluid.

$$v(t) = \frac{(\rho_p - \rho)Vg}{b}\left(1 - e^{-bt/m}\right), \text{ with constant } b = 3\pi\mu d. \tag{34}$$

Since we are interested in a range of particle Reynolds numbers, not just at the Stokes limit, we also consider the Di Felice drag force, Eq. (32), which is valid for higher Reynolds numbers and varying porosity (i.e. it considers the interaction of multiple particles). When the buoyancy and gravity force on the falling particle balance out the drag force, the particle is falling at its terminal velocity. Equating these terms leads to a polynomial equation in terms of the particle Reynolds number at terminal velocity

$$0.392Re_p^2 + 6.048Re_p^{1.5} + 23.04Re_p - \frac{4}{3}Ar\epsilon^{1+\xi} = 0, \tag{35}$$

where ξ is given in Eq. (32) and $Ar = d^3\rho(\rho_p - \rho)g/\mu^2$ is the Archimedes number. The Archimedes number gives the ratio of gravitational forces to viscous forces. A high Ar means that the system is dominated by convective flows generated by density differences between the fluid and solid particles (e.g. Buoyancy, Rayleigh Taylor instabilities) . A low Ar means that viscous forces dominate and the system is governed by external forces only.

Solving for Re_p, one can find the expected terminal velocity using $Re_p = \rho|\mathbf{u}_t|d/\mu$.

Note that a range of porosities is used for test cases CPB and RTI, and this results in a range of particle Reynolds numbers as the terminal velocity depends on the porosity.

Table 1: Relevant parameters and timescales for the simulations using different fluids. Parameters appearing only in one column are kept constant for all fluids.

	Notation	**Units**	**Air**	**Water**	**Water + 10% Glycerol**
Box Width	w	m	4×10^{-3}		
Box Height	h	m	6×10^{-3}		
Fluid Density	ρ	kg/m^3	1.1839	1000	1150
Fluid Viscosity	μ	Pa $\cdot$ s	1.86×10^{-5}	8.9×10^{-4}	8.9×10^{-3}
Particle Density	ρ_p	kg/m^3	2500		
Particle Diameter	d	m	1.0×10^{-4}		
Spring Stiffness	k	kg/s^2	1.0×10^{-4}		
Spring Damping	β	kg/s	0		
Porosity	ϵ		0.6-1.0		
Calculated Terminal Velocity (Eq. 35)	$\lvert\mathbf{u}_t\rvert$	m/s	0.102-0.5	1.3×10^{-3}-7.6×10^{-3}	1.3×10^{-4}-8.4×10^{-4}
Calculated Terminal Re Number (Eq. 35)	Re_p		0.65-3.19	0.15-0.85	0.002-0.011
Archimedes Number	Ar		83.89	18.57	0.192
Particle Contact Duration	t_c	s	2.54×10^{-3}		
Fluid CFL Condition	t_f	s	1.4-4.5 $\times 10^{-5}$		
Fluid-particle Relaxation Time	t_d	s	7.47×10^{-2}	1.56×10^{-3}	1.56×10^{-4}

Also included in Table 1 are the relevant timescales for the simulations. The particle contact duration t_c and fluid CFL condition t_f are described in Sections 3.2 and 3.1 respectively. The fluid-particle relaxation time is the characteristic time that a falling particle in Stokes flow will converge to its terminal velocity. This is given by $t_d = m/b$ from Eq. (34). This relaxation time provides another minimum timestep for the SPH-DEM simulation, given by

$$\Delta t_{relax} \leq \frac{1}{20}\frac{m}{b}. \tag{36}$$

The physical properties of the solid DEM particles are constant over all the simulated cases. Since the results of the test cases are insensitive to the particle-particle contacts, a relatively low spring stiffness of $k = 10^{-4}\text{kg/s}^2$ was used. This value ensures that the timestep is limited by the fluid CFL condition, rather than the DEM timestep, significantly speeding up the simulations.

5. Single Particle Sedimentation (SPS)

This section describes the results from SPH-DEM simulations using the first test case (SPS). We tested one and two-way coupling between the phases, the effect of different drag laws (Stokes and Di Felice), different fluid properties (air, water and water-glycerol) and the effect of varying the fluid resolution.

5.1. One and two-way coupling in Stokes flow

For a single particle falling in Stokes flow the standard Stokes drag equation, Eq. (28), can be used for the drag. Since Stokes drag law assumes a quiescent fluid, the force on the fluid due to the particle is set to zero ($\mathbf{f}_a = 0$ in Eq. (26)). This implements a one-way coupling between the phases. Note that the SPH particles can still interact with the DEM particles through the porosity field, but for a single particle this effect will be negligible.

In Figure 4 the evolution of a DEM particle's vertical speed in water is shown for one-way and two-way coupling. Also shown is the expected analytical prediction using Eq. (34). The falling DEM particle reproduces the analytical velocity very well for both one-way and two-way coupling and the error between

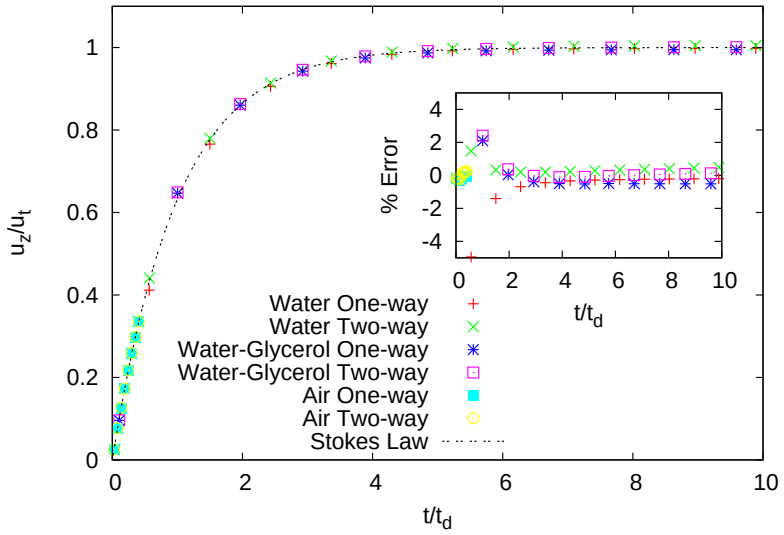

Figure 4: Sedimentation velocity for a single particle in different fluids falling from rest with both one-way and two-way coupling. The dashed line is the theoretical result integrating Stokes law. The y-axis shows the particle vertical velocity scaled by the expected terminal velocity $|\mathbf{u}_t|$ and the x-axis shows time scaled by the drag relaxation time t_d. The inset shows the percentage error between the SPH-DEM and the expected trajectory.

the two curves is less than 2% for the vast majority of the simulations. Note that the error curve does diverge to 5% when the particle is first released, but this is is a short-lived effect and the error drops below 2% after a time of about t_d, the relaxation time for the drag force.

These results indicate that the pressure gradient calculated from the SPH model, very accurately reproduces the buoyancy force on the particle, balancing out the drag force at the correct terminal velocity. The results are identical for both one-way and two-way coupling, indicating that the drag force on the fluid has a negligible effect. This is true as long as the fluid resolution is sufficiently larger than the DEM particle diameter, and this is explored in more detail in Section 5.2.

Figure 4 also shows the same result for a DEM particle falling in air and in the water-glycerol mixture. For air, the drag force on the particle is much lower than for water, and the particles do not have time to reach their terminal

velocity before reaching the bottom boundary, where the simulation ends. As for the previous simulation with water, there is initially a larger (approx 4%) underestimation of the particle vertical speed, but once again this occurs only for a very small time period and does not affect the long term motion of the particle. For the majority of the simulation the error is less than 0.3% for both one-way and two-way coupling.

The results for the water-glycerol fluid are qualitatively similar to water. Here the drag force on the particle is much higher than for water and the particle reaches terminal velocity very quickly. However, as long as the simulation timestep is modified to resolve the drag force relaxation time t_d as per Eq. (36), the results are accurate. For both the one-way and two-way coupling, the simulated velocity matches the analytical velocity very well and the error remains less than 0.3% for the duration of the simulation.

In summary, the results for the one-way and two-way coupling between the fluid and particle for all the reference fluids are very accurate, and reproduce the analytical velocity curve within 0.3-2% error besides short-lived higher deviations at the initial onset of motion. All data can scale using u_t and t_d for velocity and time respectively.

5.2. Effect of Fluid Resolution

In this section we vary the fluid resolution to see its effects on the SPS results. Using water as the reference fluid, four different simulations were performed with the number of SPH particles was ranging from 10x10x15 particles to 40x40x60. Using the SPH smoothing length h as the resolution of the fluid, this gives a range of $1.5d \leq h \leq 6d$, where d is the DEM particle diameter.

Figure 5 shows the percentage difference between the average terminal velocity of the particle and the expected Stokes law. The error bars in this plot show one standard deviation of the fluctuations in the terminal velocity around the average.

The $h/d = 6$ resolution corresponds to that used in the previous one and two-way coupled simulation, and the percentage error here is similar to the one-way

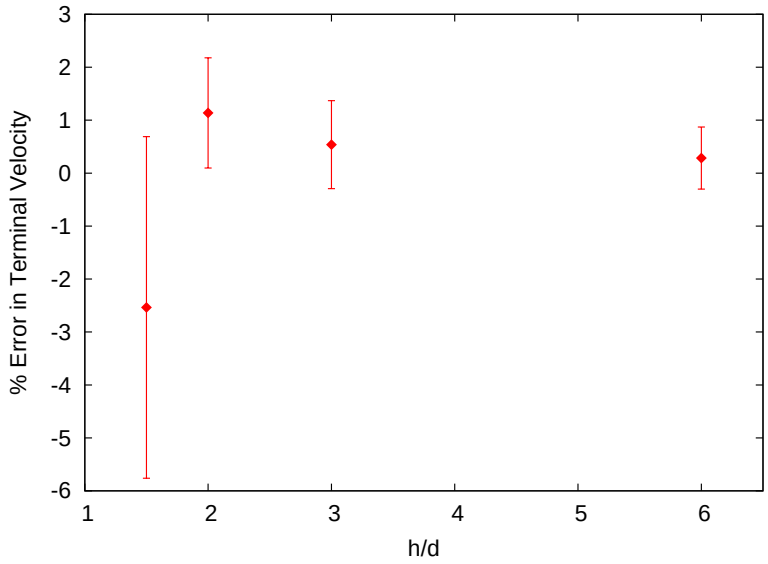

Figure 5: The effect of fluid resolution for the SPS test case, with water as the surrounding fluid. The x-axis is h/d, where h is the SPH resolution and d is the DEM particle diameter. The y-axis shows the average percentage error between the particle terminal velocity and the analytical value. The errorbars show one standard deviation from the mean.

case, which is a mean of 0.2% with a standard deviation of 0.8%. As the fluid resolution is increased there is no clear trend in the average terminal velocity, but there is an obvious increase in the fluctuation of the terminal velocity around this mean. For $h/d \geq 2$, the standard deviation of this fluctuation is less than 1%, but this quickly grows to 3% for $h/d = 1.5$.

The increased error as the fluid resolution approaches the particle diameter is due to one of the main assumptions of the AVNS equations, i.e. that the fluid resolution length scale is sufficiently larger than the solid particle diameter. In this case the smoothing operator used to calculate the porosity field is also much greater than the particle diameter and this will result in a smooth porosity field. As the fluid resolution is reduced to the particle diameter the calculated porosity field will become less smooth and there will emerge local regions of high porosity at the locations of the DEM particles. As the fluctuations in the porosity field become greater this in turn will cause greater fluctuation in the forces on the SPH particles leading to a more noisy velocity field.

Another trend, that is not clear in these results but can be seen for solid particles with higher density, is the terminal velocity of the particle increasing with increasingly finer fluid resolution. Due to the two-way coupling, the drag force on the particle will be felt by the fluid as an equal and opposite force. This will accelerate the particles by a amount proportional to the relative mass of the SPH and DEM particles. For higher resolutions the mass of the SPH particles is lower, leading to an increase in vertical velocity of the affected fluid particles. Since the DEM particle's drag force depends on the velocity difference between the phases, which is now smaller, this will lead to a increase in the particle's terminal velocity. For the SPS test case shown here, the single particle does not exert too much force on the fluid and this is not a very large effect. As the fluid resolution is decreased from $h/d = 6$ to 2, there is a slight increase (on the order of 1-2%) in the terminal velocity, but lower than this the trend is lost, likely due to the increasingly noisy results due to the fluctuations in the porosity field.

5.3. The effect of fluid properties and particle Reynolds number

We have used three different reference fluids in the simulations, corresponding to air, water and a water-glycerol mixture. Using the SPS test case, this results in a range of particle Reynolds numbers between 0.011 (water-glycerol) and 3.19 (air), allowing us to explore a realistic range of particle Reynolds numbers. We have further extended this range by considering two additional (artificial) fluids with a density of water but lower viscosities, resulting in a range of $0.011 \leq Re_p \leq 9$.

Rather than assuming Stokes flow as in the previous sections, here we will use the Di Felice drag law ($\epsilon = 1$), which is assumed to be valid for all Reynolds numbers. This will be compared against fully resolved simulations using COMSOL Multiphysics (finite element analysis, solver and simulation software. `http://www.comsol.com/`).

Figure 6 shows the average error in the terminal velocity measured from the SPH-DEM simulations using both the Stokes and Di Felice drag laws, using the COMSOL results as the reference terminal velocity. Since the two drag laws

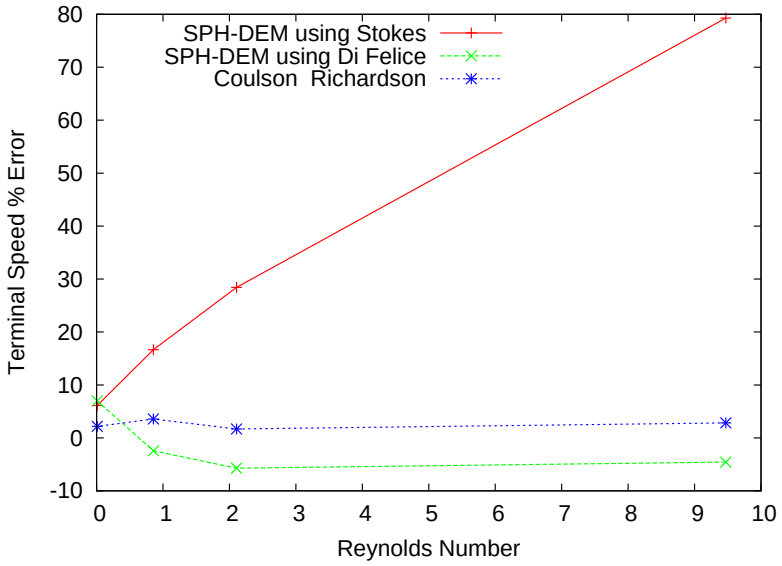

Figure 6: Error in SPH-DEM average SPS terminal velocity at different terminal Re numbers. The fully resolved COMSOL simulation is used as reference for the error calculation. The solid red and dashed green lines show the results using either Stokes or Di Felice drag law. The dotted blue line shows the reference terminal velocity calculated using the Coulson and Richardson drag law (Coulson and Richardson, 1993).

are equivalent at low Re_p, they give the same result at $Re_p = 0.01$. As Re_p increases, the plots diverge, and the simulated terminal velocity using the Stokes drag quickly becomes much larger than the COMSOL prediction (as expected since the Stokes drag law is only valid for low Re_p). In contrast, the Di Felice drag law results in a simulated terminal velocity that follows the same trend as the COMSOL results. At low Re_p the DEM particle falls slightly ($\sim 5\%$) faster, at higher Re_p it falls slightly (3-6%) slower.

For further comparison, the COMSOL results have also been compared with the analytical drag force model proposed by Coulson and Richardson and reproduced in Eq. (29). The expected terminal velocity was calculated using this model and plotted alongside the SPH-DEM results in Figure 6. As shown, the COMSOL results agree with this analytical terminal velocity to within 3.5% over the range of Re_p considered.

While the results in previous SPS sections have shown the SPH-DEM model

can accurately reproduce the expected terminal velocity assuming a given drag law (Stokes), this section illustrates that the final accuracy is still largely determined by the suitability of the underlying drag law chosen. However, a full comparison of the numerous drag laws currently in the literature is beyond the scope of this paper, and for the purposes of validating the SPH-DEM model we can assume that the chosen drag law (from here on the Di Felice), approximates well the true drag on the particles.

6. Sedimentation of a Constant Porosity Block (CPB)

This section shows the results from the Constant Porosity Block (CPB) test case. In a similar fashion to the SPS case, we explore the effect of fluid resolution and fluid properties. In addition, we consider the influence of a new parameter, the porosity of the block, on the results. All the simulations in this section use two-way coupling, as the hindered fluid flow due to the presence of the solid particles is an important component of the simulation. As the porous block falls, the fluid will be displaced and flow upward through the block, affecting the terminal velocity. All the simulations use the Di Felice drag law, which is necessary to incorporate the effects of neighbouring particles (lower porosity) on the drag force.

Figure 7 shows an example visualisation during the simulation of a block with porosity $\epsilon = 0.8$ falling in water. On the left hand side of the image are the DEM particles (coloured by porosity ϵ_i) falling in the fluid column. The porosity of most of the DEM particles is $\epsilon = 0.8$, as expected, except near the edge of the block where the discontinuity in particle distribution is smoothed out by the kernel (with smoothing length $h_c \cong 6d$) in Eq. (9). This results in a porosity greater than 0.8 for DEM particles whose distance is lower than h_c from the edge of the block. We will show in Section 6.1 that this effect can be limited/avoided by choosing a smaller smoothing length.

On the right hand side is shown a vector plot of the velocity field at $x = 0$. This shows the upward flow of fluid due to the displacement of fluid by the

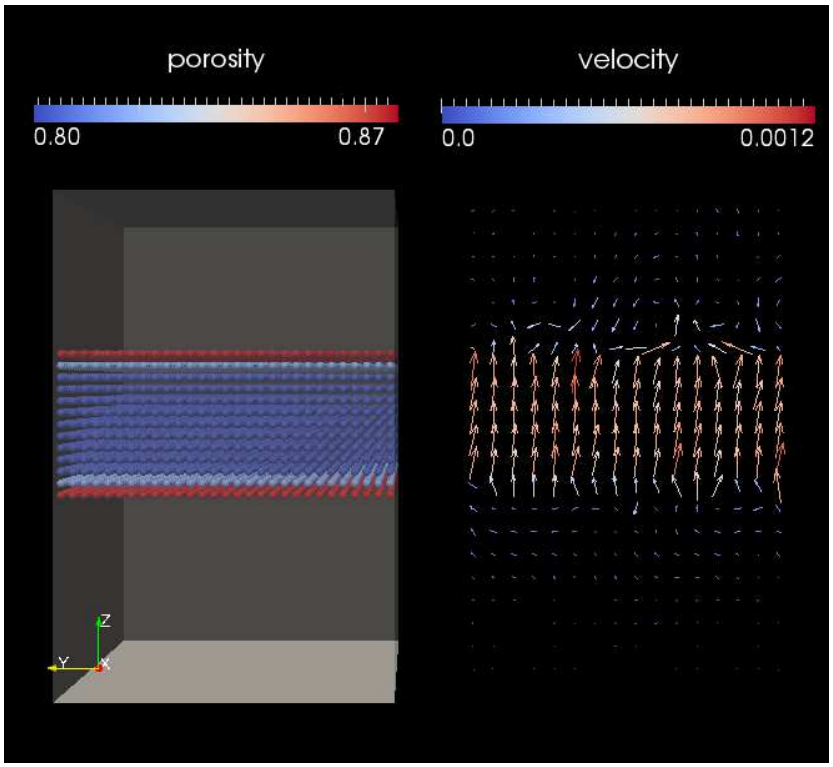

Figure 7: Visualisation of the DEM particles for the Constant Porosity Block test case. On the left the DEM particles are shown coloured by porosity ϵ_i, and a transparent box representing the simulation domain. On the right the corresponding fluid velocity field is shown at $x = 0$, with the arrows scaled and coloured by velocity magnitude.

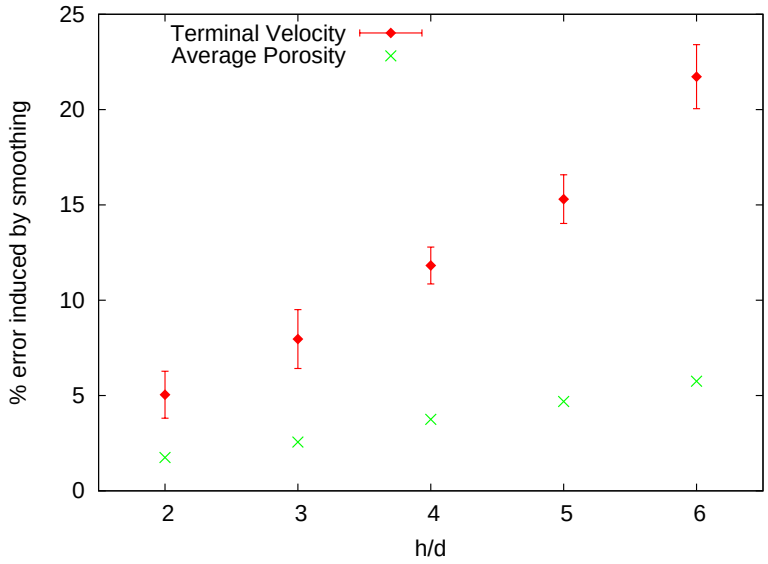

Figure 8: Average percentage change in the terminal velocity and average porosity of the Constant Porosity Block (CPB) with $\epsilon = 0.8$ in water for varying fluid resolution. Errorbars in the terminal velocity points show one standard deviation of the vertical velocity data from the average, taken over a time period of 0.34 s after the terminal velocity has been reached.

particles as they fall. Also noticeable are fluctuations in velocity near the edges of the block, which are discussed in more detail in Section 6.3.

Shortly after release, the vertical velocity of the CPB converges to a terminal velocity that is consistent with the expected terminal velocity, although it is slightly (less than 5%) higher than expected. The systematically increased terminal velocity is due to reduced drag at the edges of the block due to the finite width of the smoothing kernel. As the width of the smoothing kernel h used to calculate the porosity field is larger (by a factor of 2-6, see Figure 8 for details) than the particle diameter d, the porosity field near the edges of the CPB will be smoothed out according to the width of the kernel. This results in a slightly higher apparent local porosity and a reduced drag than what would be expected with $\epsilon = 0.8$.

6.1. The effect of fluid resolution

Figure 8 shows the percentage difference between the vertical velocity of the block and the expected terminal velocity. The results from five different

simulations are shown, each with a different fluid resolution ranging from $h/d = 6$ to $h/d = 2$. The porosity is set to $\epsilon = 0.8$. The $h/d = 6$ plot uses a smoothing kernel that is 6 times greater than the DEM particle diameter, leading to increasing smoothing of porosity field near the edges of the block. Integrated the porosity field over the volume of the CPB leads to a porosity of 0.85, about 6% higher than the true porosity of the block. This results in an increase of 22% in the terminal velocity of the block. Increasing the fluid resolution to $h/d = 5$ causes the error to decrease to 15%, since the interpolated porosity at the edge of the block is now closer to the set value of $\epsilon = 0.8$. Further increases in the fluid resolution consistently decreases the measured terminal velocity until at $h/d = 2$ the error is only 5% of the expected value. These results illustrate how the smoothing applied to the porosity field can have dramatic results on the accuracy of the simulations. This is largely due to the fact that the modelled drag only depends on the local porosity, which does not properly consider the influence of porosity gradients on the applied drag force. Therefore the accuracy of the drag law near large changes in porosity is highly dependent on the magnitude of smoothing applied to the porosity field. This is true for the Di Felice law and the most other drag laws proposed in the literature, but there has been some recent work by Xu et al. (2007), which attempts to account for the influence of the porosity gradient, but we will not study this further here.

6.2. The effect of porosity

Varying the porosity of the CPB allows us to evaluate the accuracy of the SPH-DEM model at different porosities. Figure 9 shows the average terminal velocity of the block, as measured from SPH-DEM simulation of the CPB over a range of porosities from $\epsilon = 0.6$ to 1.0. Results using both water and water-glycerol as the interstitial fluid are shown on the same plot by scaling the y-axis by the expected terminal velocity of a single DEM particle. The average terminal velocity is taken after the block has reached a steady terminal velocity and the error bars show one standard deviation of the vertical velocity from the average. For these simulations, again $h/d = 2$ is used.

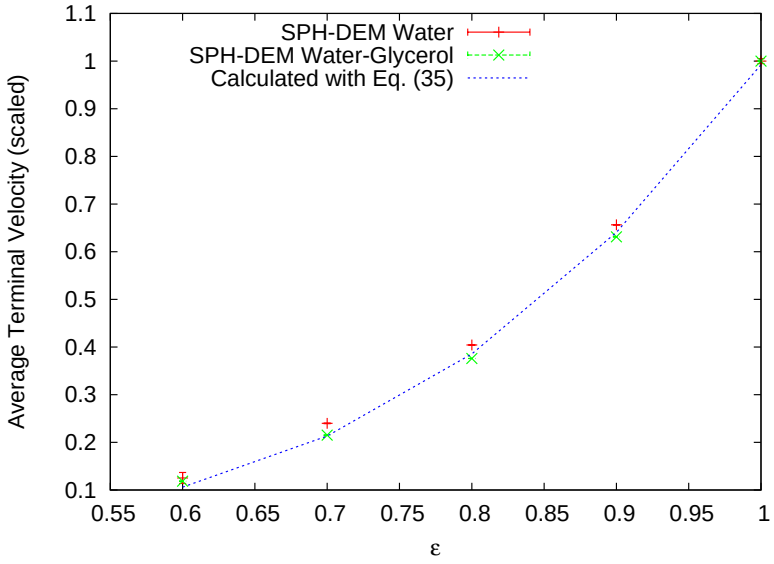

Figure 9: Average terminal velocity (scaled by $|\mathbf{u}_t|$, the expected terminal velocity of a single DEM particle) of the Constant Porosity Block (CPB) in water and water-glycerol for varying porosity and $h/d = 2$. Errorbars show one standard deviation of the vertical velocity data from the average, taken over a time period of 0.34 s. The y-axis is scaled by $|\mathbf{u}_t|$, the expected terminal velocity of a single DEM particle given by Eq. (35), which corresponds to the SPS test case.

Shown with the SPH-DEM results is a reference line showing the expected terminal velocity computed using Eq. (35) and the input porosity of the block. The SPH-DEM results for both water and water-glycerol match this reference line very well over the range of porosities tested. At lower porosities the vertical velocity of the CPB suffers from increasing fluctuation around the mean. This is a consequence of fluctuations seen in the surrounding fluid velocity, and will be described further in Section 6.3.

In summary, the simulated terminal velocity for the CPB matched the expected value over the range of resolutions and porosities considered, as long as the resolution of the fluid phase (give by h) is sufficient to resolve the porosity field of the given problem. For the CPB we have a jump at the edge of the block from the given porosity of the block to the surrounding $\epsilon = 1$. We found that as long as the fluid resolution was kept at $h = 2d$, where d is the DEM particle diameter (i.e.. the length scale of the porosity jump), the results matched the theoretical predictions within 5% error.

6.3. Effect of Porosity Gradients on Fluid Solution

In the previous section it was shown how the smoothing of the porosity discontinuity of the block slightly affected the drag on the DEM particles and the final terminal velocity of the block. In this section we will show how the high porosity gradients near the edge of the block also gave rise to further effects on the SPH solution for the fluid.

Figure 10 shows the vertical velocity and porosity for all the SPH particles in a CPB simulation with fluid resolution $h/d = 2$ and porosity $\epsilon = 0.8$. These values are plotted against the vertical position of the SPH particles. The porosity is rather smooth and clearly shows the location of the CPB. However, there are fluctuations in the vertical velocity of the SPH particles near the edges of the block, much larger than the rather small average (positive) velocity inside the block. These fluctuations are present to different degrees in all of the SPH-DEM simulations and their magnitude is proportional to the local porosity gradient. Therefore, their effect is strongest for the simulations with low porosity or fine

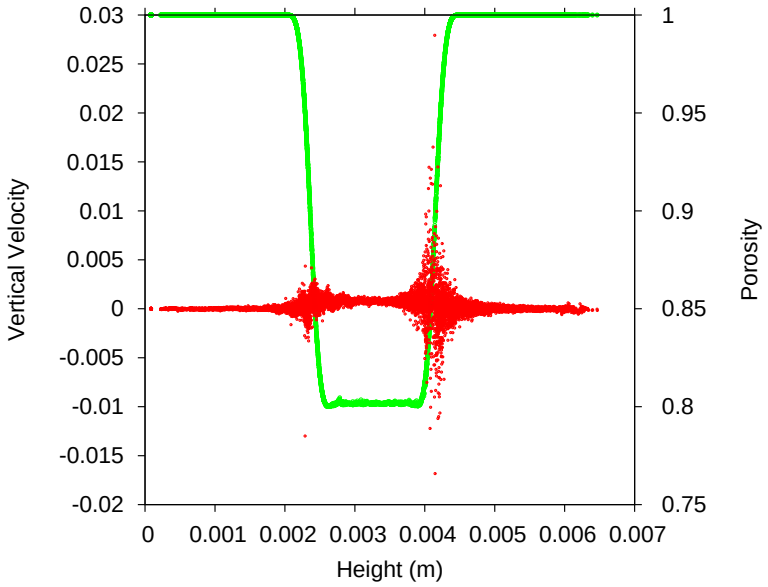

Figure 10: Scatter-plot of the vertical velocity (red dots) and porosity (green line) versus height for all the SPH particles. The test case was CPB with a porosity of $\epsilon = 0.8$ in water as the surrounding fluid, the fluid resolution was $h/d = 2$ and $\alpha_{art} = 0.1$

fluid resolution (i.e. small h_c).

Given the correlation of these fluctuations with high porosity gradients, their source is likely to be due to errors in the SPH pressure field. It is well-known (e.g. (Colagrossi and Landrini, 2003)) that SPH solutions can exhibit spurious fluctuations in the pressure field, which normally have little or no effect on the fluid velocity. For our simulations the pressure of each SPH particle is proportional to $(\rho/\epsilon\rho_0)^7$ and is therefore very sensitive to changes in ϵ. It is likely that for high porosity gradients the pressure variations that are normally present would be amplified and generate corresponding large fluctuations in the velocity field.

As long as the fluctuations do not grow too large, they do not effect the mean flow of the fluid, as evidenced by the accurate reproduction of the expected terminal velocity in the previous sections. To ensure the simulation accuracy, it was found that the application of an artificial viscosity with strength $\alpha_{art} = 0.1$, see Eq. (13), was enough to damp out the fluctuations in velocity so that they

did not have a significant effect on the results. This value of α_{art} was used in all of the CPB simulations shown here. The artificial viscosity has no effect on the settling velocity of the SPS or CPB since this viscosity is only applied between SPH particles and is not included in the fluid-particle coupling term (Eq. 23). However, for systems where the fluid viscosity plays an important role (e.g. the Rayleigh Taylor instability in the following section), this has an effect which will be described in the next section.

7. Rayleigh-Taylor Instability (RTI)

The classic Rayleigh-Taylor fluid instability is seen when a dense fluid is accelerated into a less dense fluid, for example, under the action of gravity. Consider a water column of height h filled with a dense fluid with density ρ_d and viscosity ν_d located above a lighter fluid with parameters ρ_f and ν_f. For the RTI test case, the lower and higher density fluids are represented by the pure fluid and the suspension, respectively. If the height of the interface between the two fluids is perturbed by a normal mode disturbance with a certain wave number k (see Figure 11 and Eq. (39)), then this disturbance will grow exponentially with time.

The two-fluid model of a Rayleigh-Taylor instability was derived in the authoritative text by Chandrasekhar (1961). The exponential growth rate $n(k)$ of a normal mode disturbance with wave number k at the interface between the two fluids (with zero surface tension) is characterised by the dispersion relation (Chandrasekhar, 1961) given by

$$\begin{aligned}
&- \left[\frac{gk}{n^2}(\alpha_f - \alpha_d) + 1\right](\alpha_c q_d + \alpha_f q_c - k) - 4k\alpha_f\alpha_d \\
&+ \frac{4k^2}{n}(\alpha_f\nu_f - \alpha_d\nu_d)[\alpha_d q_f - \alpha_f q_d + k(\alpha_f - \alpha_d)] \\
&+ \frac{4k^3}{n^2}(\alpha_f\nu_f - \alpha_d\nu_d)^2(q_f - k)(q_d - k) = 0, \qquad (37)
\end{aligned}$$

where $\nu_{f,d} = \mu_{f,d}/\rho_{f,d}$ is the kinematic viscosity of the two phases, $\alpha_{f,d} =$

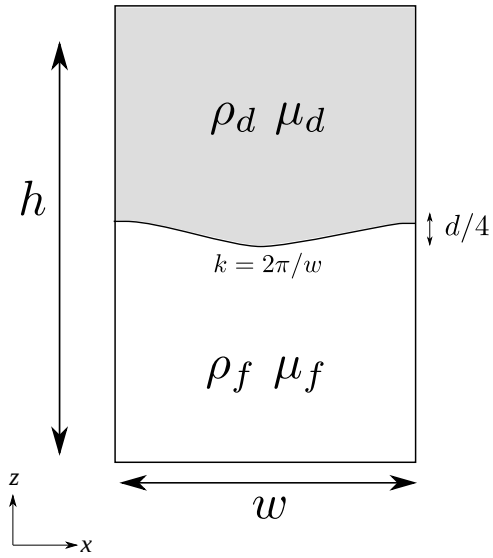

Figure 11: Diagram showing a cross-section of the initial setup for the Rayleigh-Taylor Instability (RTI) test case. The upper grey area is the particle-fluid suspension with effective density and viscosity ρ_d and μ_d, the lower white region is clear fluid with density and viscosity ρ_f and μ_f. The suspension is given an initial vertical perturbation with wave number k and amplitude $d/4$.

$\rho_{f,d}/(\rho_f + \rho_d)$ is a density ratio and $q^2_{f,d} = k^2 + n/\nu_{f,d}$ is a convenient abbreviation.

For this test case, we use an identical initial condition as in the CPB test case, with an initial block of particles immersed in the fluid with an initial porosity of $\epsilon = 0.8$. Using the density of the surrounding fluid ρ_f, the effective density of the fluid-particle suspension is $\rho_d = \epsilon\rho_f + (1-\epsilon)\rho_p$. This system can be approximated using a two fluid model, where the suspension is treated as a fluid with density ρ_d and kinematic viscosity ν_d. Therefore, in a similar fashion to the RT instability described above, it is expected that an initial disturbance of the interface between the two "fluids" will increase with an exponential growth rate which is a solution of Eq. (37).

The effective viscosity of the suspension μ_d is estimated here using Krieger's hard sphere model (Krieger, 1959) (assumed to be valid for both dilute and dense suspensions)

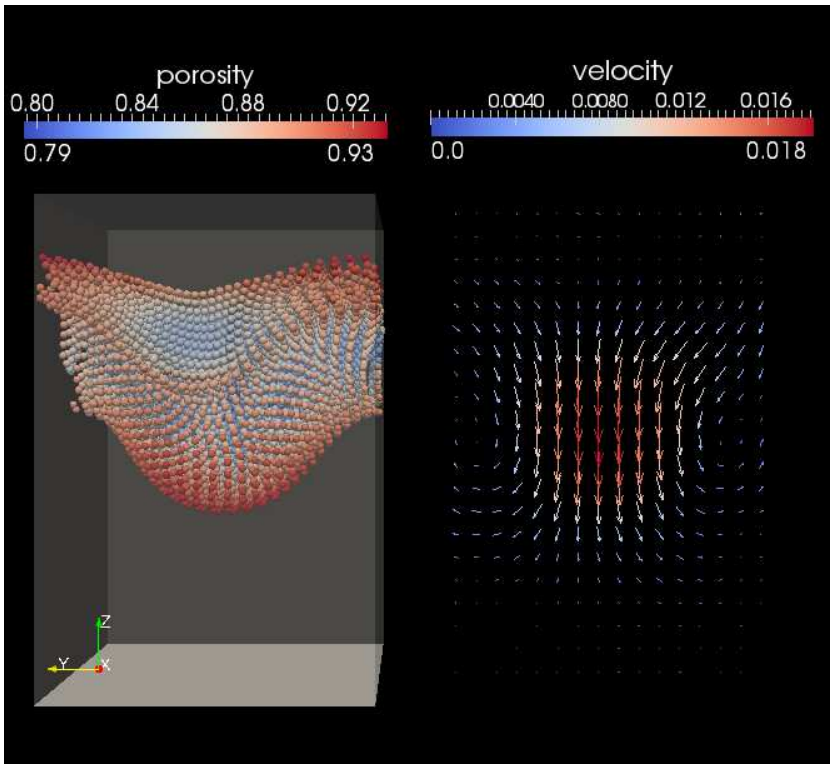

Figure 12: Visualisation of the DEM particles (left) and velocity field (right) at $x = 0$ in the x-z plane, for the Rayleigh Taylor (RT) test case, using $\epsilon = 0.8$ and water-glycerol as the surrounding fluid. The growth rate for this simulations versus time can be seen in Figure 14.

$$\mu_d = \mu_f \left(\frac{\epsilon - \epsilon_{min}}{1 - \epsilon_{min}} \right)^{-2.5(1-\epsilon_{min})}, \tag{38}$$

where $\epsilon_{min} = 0.37$ is the porosity at the maximum packing of the solid particles.

We generate an initial disturbance in the interface between the two "fluids" by adding a small perturbation to the vertical position of every DEM particle

$$\Delta z_i = -\frac{d}{4}(1 - \cos(k_x x_i))(1 - \cos(k_y y_i)), \tag{39}$$

where $k_x = k_y = 2\pi/w$ and x_i and y_i are the x- and y-coordinates of the position of particle i. This yields a symmetric disturbance in the interface with a wave length equal to the box width w.

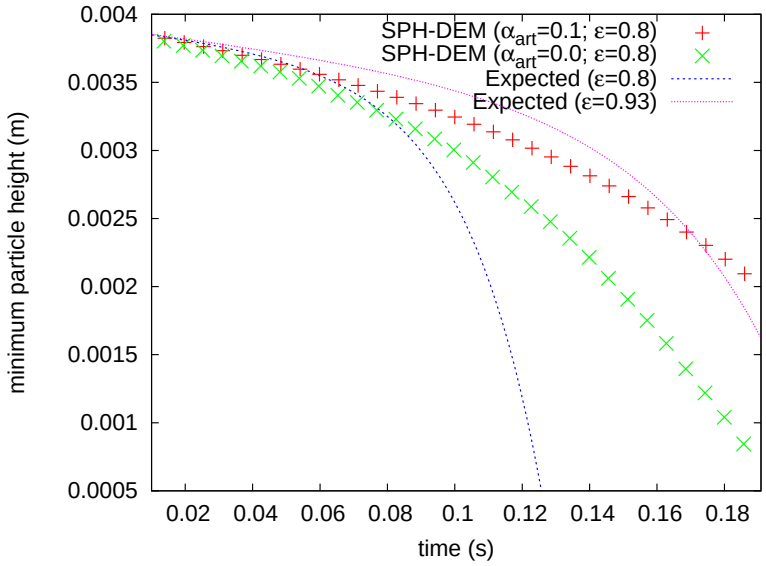

Figure 13: Growth of Rayleigh-Taylor instability using water. The red pluses and green crosses show the position of the lowest DEM particle when the artificial viscosity is either added or not. The two reference lines show the expected growth rate using the lowest and highest porosity of the CPB.

Figure 12 shows the positions of the DEM particles during the growth of the instability, along with the fluid velocity field at $x = 0$. At this time there is a strong fluid circulation that is moving downward in the centre of the domain and upward at the edges (not visible in this cut). This causes the growth of the instability by increasing the sedimentation speed of the DEM particles near the centre while reducing or even reversing the sedimentation of those particles near the outer boundaries of the domain. The movement of the DEM particles matches the expected behaviour of the instability, and the wave length of the dominant mode is identical to the initial perturbation given to the DEM particle positions. Next we will attempt to quantitatively compare the SPH-DEM results to the growth rate predicted by the analytical two-fluid model.

In Figure 13 the growth of the RT instability versus time for $\epsilon = 0.8$, fluid resolution $h/d = 2$ is shown using water as the surrounding fluid. The symbols show the vertical position of the lowest DEM particle, which provides an approximate measure of the instability amplitude. The vertical displacement of

this point over time can be compared with the estimated growth rate for the RT instability as given by the two-fluid model in Eq. (37). The growth rate of the instability is added to the expected sedimentation speed using Eq. (35) to calculate the expected trajectory of the lowest DEM particle. Using the parameters of the simulation (including $\epsilon = 0.8$) and solving for the growth rate leads to a growth curve given by the lowest blue dashed line. The two-fluid model is included here as a benchmark, but it should be noted that this model contains some significant approximations in treating the particle suspension as an equivalent fluid, and is not necessarily more accurate than the SPH-DEM results. While a constant porosity of 0.8 is used for the two-fluid RTI model, the porosity of the DEM particles ranges from $0.8 \leq \epsilon \leq 0.86$ at $t = 0$ (initial conditions) and the porosity at the leading front of the instability grows over time, reaching a value of 0.93 at the timestep shown in Figure 12 and a maximum value of 0.95 before the instability meets the bottom boundary. To account for this variation in porosity, we instead use the analytical model to obtain an upper and lower bound to the instability growth. The upper bound is calculated using $epsilon = 0.8$ (the blue dashed line) and the upper bound is calculated using $\epsilon = 0.93$, which gives the purple dashed line.

The SPH-DEM results are shown for the cases where the artificial viscosity is either applied ($\alpha_{art} = 0.1$) or not used ($\alpha_{art} = 0.0$). In both cases there is a clear exponential growth of the RT instability and only the quantitative growth rate differs between the two simulations. If the artificial viscosity is applied, the growth rate of the instability is lower than both of the two reference bounds. If the artificial viscosity is not used, the growth rate of the instability is increased to lie between the two bounds. After $t = 0.15$ s the growth rate becomes slower than the upper bound, but by this time the bottom of the instability is close to the bottom boundary, and we do not expect the two-fluid model (which assumes an unbounded domain) to apply.

Figure 14 shows the same results but using water-glycerol as the interstitial fluid. In this case the physical viscosity of the fluid is proportionally greater than the artificial viscosity applied, and therefore the addition of the artificial

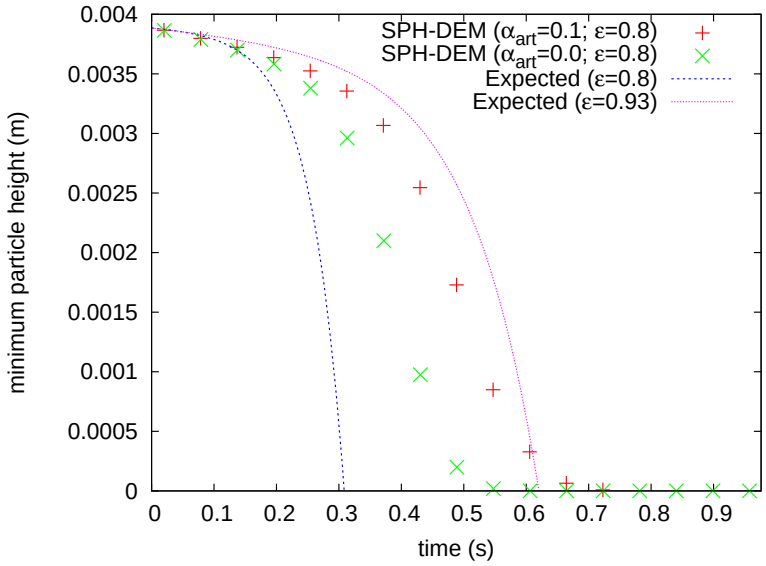

Figure 14: Growth of Rayleigh-Taylor instability using water-glycerol. The red pluses and green crosses show the position of the lowest DEM particle when the artificial viscosity is either added or not. The two reference lines show the expected growth rate using the lowest and highest porosity of the CPB.

viscosity has a lesser effect. For both $\alpha_{art} = 0.1$ and $\alpha_{art} = 0.0$ the growth rate of the instability lies between the two bounds, except when the DEM particles reach the bottom of the domain and wall effects start to dominate.

While it is encouraging that the SPH-DEM results (without artificial viscosity) closely match the expected growth of the RT instability, the results highlight the negative effect of the artificial viscosity when used in problems where the fluid viscosity is important. Therefore it is necessary to develop an alternative method of reducing the velocity fluctuations near high porosity gradients, and this is the subject of current work. However, it is important to note that for the majority of applications the addition of a small amount of artificial viscosity has no significant effect on the results and is successful in eliminating the problematic velocity fluctuations.

In summary, the results from the RTI simulations using water-glycerol show that the SPH-DEM simulation can accurately reproduce the Rayleigh-Taylor instability. The addition of an artificial viscosity, while successful in dampen-

ing the velocity fluctuations, increases the effective viscosity of the system and reduces the growth rate of the instability.

8. Conclusion

We have presented an SPH implementation of the locally averaged Navier Stokes equations and coupled this with a DEM model in order to provide a simulation tool for one or two-way coupled fluid-particle systems. One notable property of the resulting method is that it avoids the use of a mesh and is completely particle-based. It is therefore suitable for those applications where a mesh presents additional problems, for example, free surface flow or flow around complex, moving and/or intermeshed geometries (Robinson et al., 2012).

The SPH-DEM formulation was applied to 3D single and multiple particle sedimentation problems and compared against analytical solutions. For single particle sedimentation the SPH-DEM simulations reproduced the analytical solutions very well, with less than 2% error over a wide range of Particle Reynolds Number $0.011 \leq Re_p \leq 9$ and fluid resolutions. Only when the fluid resolution became less than or equal to 1.5 times the particle diameter did the results start to diverge from the expected solution.

For the multiple particle sedimentation test case using the Constant Porosity Block (CPB), the SPH-DEM method accurately reproduced the expected terminal velocity of the block, over a range of porosities $0.5 < \epsilon < 1.0$ and Particle Reynolds Number $0.002 \leq Re_p \leq 0.85$. This is a general consequence of the locally averaged Navier Stokes equation, and is not specific to the SPH-DEM method. The minimum resolution of the porosity field will always be much coarser than the DEM particle diameter, so any discontinuities in the particle distribution will be smoothed and thus not be accurately reflected in the porosity field. Furthermore, the results from the CPB also showed an instability in the SPH fluid phase that occurred near the edges of the block. The high porosity gradients in this region give rise to fluctuations in velocity of the SPH particles, which are likely due to fluctuations in the pressure field being amplified by the sudden change in porosity. Adding a small amount of artificial viscosity to the

simulations was sufficient to damp these fluctuations and prevent them from affecting the terminal velocity of the block.

The Rayleigh-Taylor Instability (RTI) test case successfully reproduced the instability and its growth rate for both water and water-glycerol. For this test case the addition of artificial viscosity was not necessary, due to the relatively high porosity $\epsilon = 0.8$ and lower porosity gradients at the interface between the suspension and clear fluid.

Removing the SPH velocity fluctuations near high porosity gradients is the subject of current work, and promising results have already been obtained by either calculating the drag separately on the fluid or re-deriving the SPH equations from a Lagrangian formulation. Besides this issue, it was found that the SPH-DEM model successfully reproduced most of the expected results from the analytical test cases over a wide range of Reynolds Numbers and porosities, and promises to be a flexible and accurate tool for modelling particle-fluid systems.

In the future, the method will be applied to dispersion of solids in fluid or fluid-gas environments (Robinson et al., 2012). Other relevant directions for future developments are: choice of drag law and the inclusion of the added mass and lift forces; the choice of DEM particle contact forces and the inclusion of friction and lubrication forces; and the inclusion of surface tension effects. These questions require further study of the method and the choice of the parameters, laws and assumptions.

Acknowledgment

This work is supported by the PARDEM (www.pardem.eu) collaboration, which is a EU Funded Framework 7, Marie Curie Initial Training Network. Thanks to use of the cluster supported by the two STW grants on "A Numerical Wave Tank for Complex Wave and Current Interactions" of Bokhove and Van der Vegt and on "Polydispersed Granular Flows through Inclined Channels" by Bokhove, Kuipers, Van der Vegt and Luding.

References

Anderson, T.B., Jackson, R., 1967. Fluid mechanical description of fluidized beds. equations of motion. Industrial & Engineering Chemistry Fundamentals 6, 527–539.

Chandrasekhar, S., 1961. Hydrodynamic and hydromagnetic stability. Dover Pubns.

Chu, K., Yu, A., 2008. Numerical simulation of complex particle-fluid flows. Powder Technology 179, 104–114.

Cleary, P., Sinnott, M., Morrison, R., 2006. Prediction of slurry transport in SAG mills using SPH fluid flow in a dynamic DEM based porous media. Minerals engineering 19, 1517–1527.

Colagrossi, A., Landrini, M., 2003. Numerical simulation of interfacial flows by Smoothed Particle Hydrodynamics. Journal of Computational Physics 191, 448–475.

Coulson, J., Richardson, J., 1993. Chemical Engineering. volume 2. 4 edition.

Dallavalle, J., 1948. Micromeritics: the technology of fine particles. Pitman, New York.

Deen, N., Van Sint Annaland, M., Van Der Hoef, M., Kuipers, J., 2007. Review of discrete particle modeling of fluidized beds. Chemical Engineering Science 62, 28–44.

Di Felice, R., 1994. The voidage function for fluid-particle interaction systems. International Journal of Multiphase Flow 20, 153–159.

Ergun, S., 1952. Fluid flow through packed columns. Chemical Engineering and Processing 48, 89–94.

Fernandez, J., Cleary, P., Sinnott, M., Morrison, R., 2011. Using SPH one-way coupled to DEM to model wet industrial banana screens. Minerals Engineering 24, 741–753.

Gingold, R.A., Monaghan, J.J., 1977. Smoothed particle hydrodynamic: theory and application to non-spherical stars. Monthly Notices of the Royal Astronomical Society 181, 375–389.

Van der Hoef, M., Beetstra, R., Kuipers, J., 2005. Lattice-Boltzmann simulations of low-Reynolds-number flow past mono-and bidisperse arrays of spheres: results for the permeability and drag force. Journal of fluid mechanics 528, 233–254.

Hoomans, B., 1996. Discrete particle simulation of bubble and slug formation in a two-dimensional gas-fluidised bed: A hard-sphere approach. Chemical Engineering Science 51, 99–118.

Hoomans, B., Kuipers, J., van Swaaij, W., 2000. Granular dynamics simulation of segregation phenomena in bubbling gas-fluidised beds. Powder Technology 109, 41–48.

Jiang, F., Oliveira, M., Sousa, A., 2007. Mesoscale SPH modeling of fluid flow in isotropic porous media. Computer Physics Communications 176, 471–480.

Krieger, I., 1959. A mechanism for non Newtonian flow in suspensions of rigid spheres. Trans. Soc. Rheol. 3, 137–152.

Li, X., Chu, X., Sheng, D., 2007. A saturated discrete particle model and characteristic-based SPH method in granular materials. Int. J. Numer. Meth. Engng 72, 858–882.

Lucy, L.B., 1977. A numerical approach to testing the fission hypothesis. The Astronomical Journal 82, 1013–1924.

Monaghan, J.J., 1997. SPH and Riemann Solvers. Journal of Computational Physics 136, 298–307.

Monaghan, J.J., 2005. Smoothed particle hydrodynamics. Reports of Progress in Physics 68, 1703–1759.

Monaghan, J.J., Kos, A., Issa, N., 2003. Fluid motion generated by impact. Journal of waterway, port, coastal and ocean engineering 129, 250–259.

Pereira, G., Prakash, M., Cleary, P., 2010. SPH modelling of fluid at the grain level in a porous medium. Applied Mathematical Modelling .

Potapov, A., 2001. Liquid solid flows using smoothed particle hydrodynamics and the discrete element method. Powder Technology 116, 204–213.

Price, D., 2012. Smoothed particle hydrodynamics and magnetohydrodynamics. Journal of Computational Physics 231, 759–794.

Robinson, M., Luding, S., Ramaioli, M., 2012. Simulations of grain dispersion by liquid injection using SPH-DEM. to be published .

Robinson, M., Monaghan, J., 2011. Direct numerical simulation of decaying two-dimensional turbulence in a no-slip square box using smoothed particle hydrodynamics. International Journal for Numerical Methods in Fluids .

Shepard, D., 1968. A two-dimensional interpolation function for irregularly-spaced data, in: Proceedings of the 1968 23rd ACM national conference, ACM. pp. 517–524.

Tsuji, Y., Kawaguchi, T., Tanaka, T., 1993. Discrete particle simulation of two-dimensional fluidized bed. Powder Technology 77, 79–87.

Wachmann, B., Kalthoff, W., Schwarzer, S., Herrmann, H., 1998. Collective drag and sedimentation: comparison of simulation and experiment in two and three dimensions. Granular Matter 1, 75–82.

Wen, C., Yu, Y., 1966. Mechanics of fluidization. Chemical Engineering Programming Symposium Series 62, 100–108.

Xu, B., 1997. Numerical simulation of the gas solid flow in a fluidized bed by combining discrete particle method with computational fluid dynamics. Chemical Engineering Science 52, 2785–2809.

Xu, B., 2000. Numerical simulation of the gas solid flow in a bed with lateral gas blasting. Powder Technology 109, 13–26.

Xu, M., Ge, W., Li, J., 2007. A discrete particle model for particle-fluid flow with considerations of sub-grid structures. Chemical engineering science 62, 2302–2308.

Zhu, Y., Fox, P., Morris, J., 1999. A pore-scale numerical model for flow through porous media. International journal for numerical and analytical methods in geomechanics 23, 881–904.